# Supporting Information for

## Iridium single atoms incorporated in $Co_3O_4$ efficiently catalyze the oxygen evolution in acidic conditions

Zhu *et al.*

## Supplementary Figures

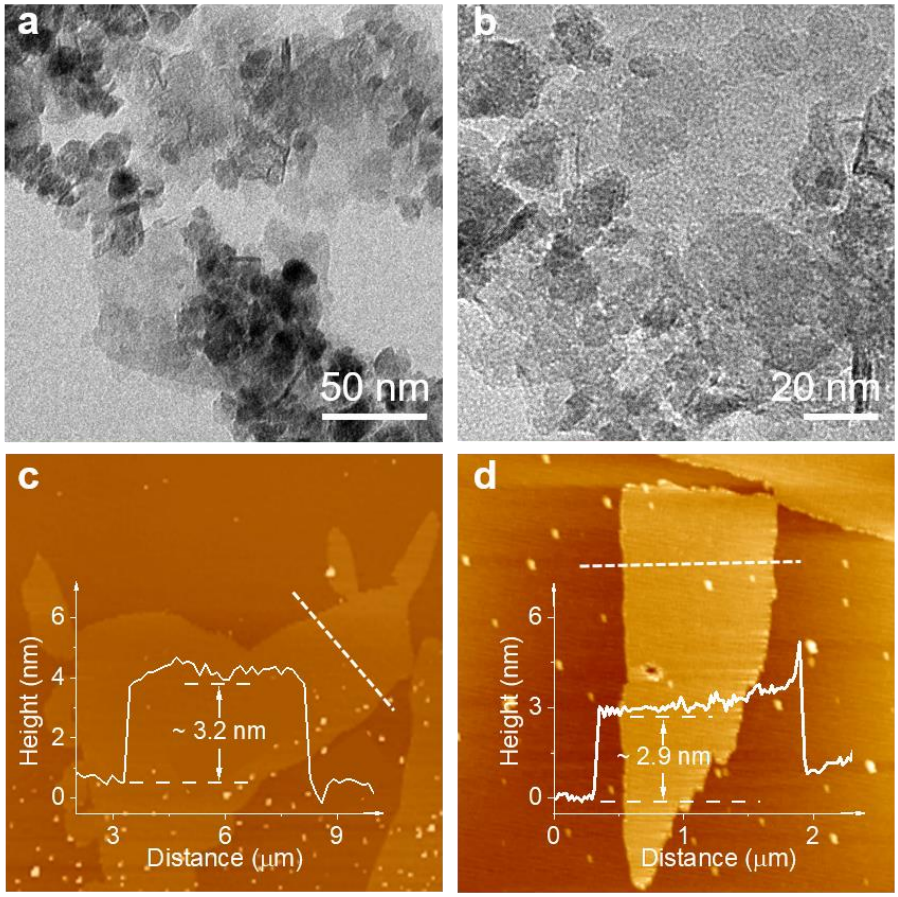


**Supplementary Figure 1**. Additional (a, b) TEM images and (c, d) AFM images for Ir-$Co_3O_4$.

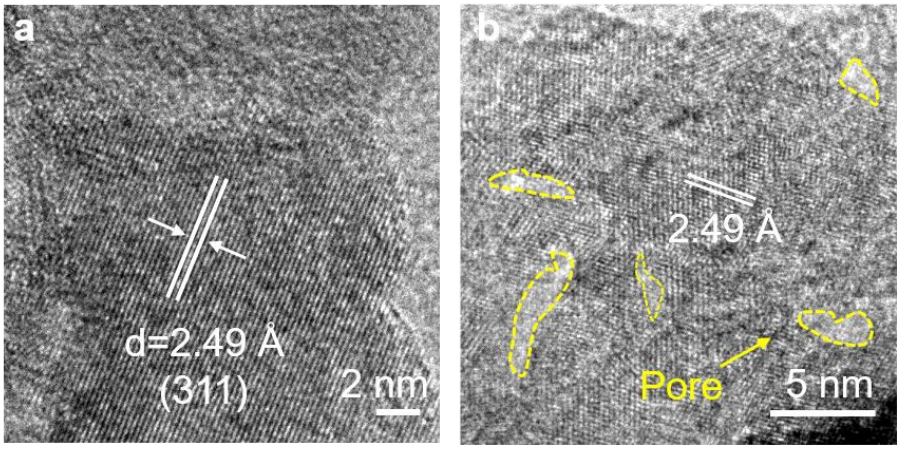


**Supplementary Figure 2**. HRTEM images of Ir-$Co_3O_4$.Yellow circles represent the defective pores on Ir-$Co_3O_4$.

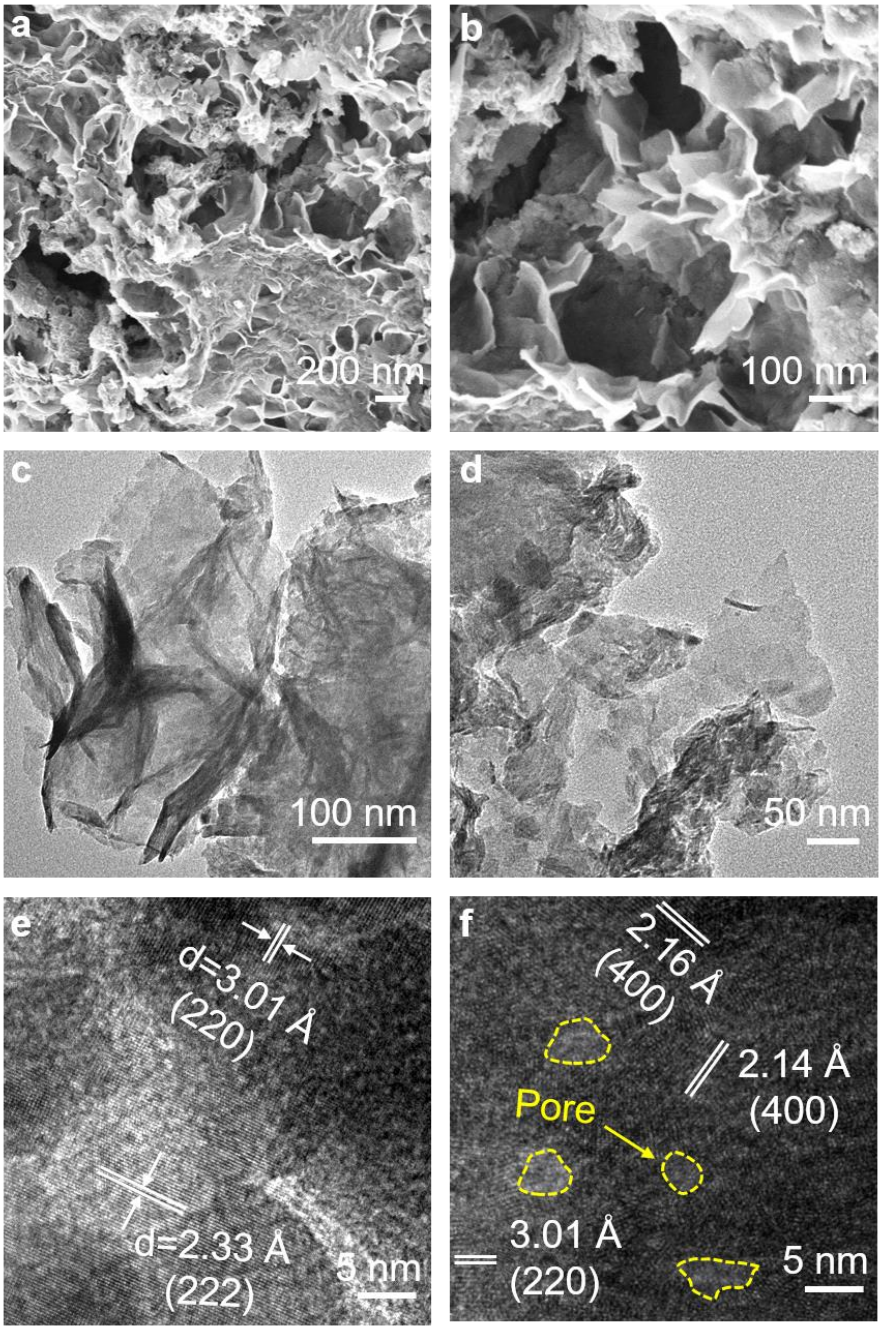


**Supplementary Figure 3.** (a, b) SEM images, (c, d) TEM images and (e, f) HRTEM images of as-synthesized $Co_3O_4$. Yellow circles represent the defective pores on $Co_3O_4$.

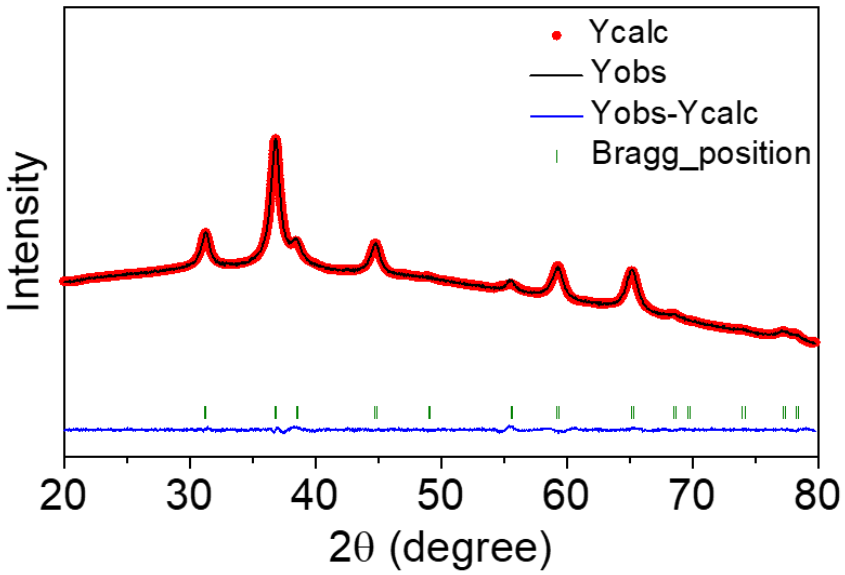


**Supplementary Figure 4**. Rietveld refinements of XRD patterns on Ir-$Co_3O_4$.

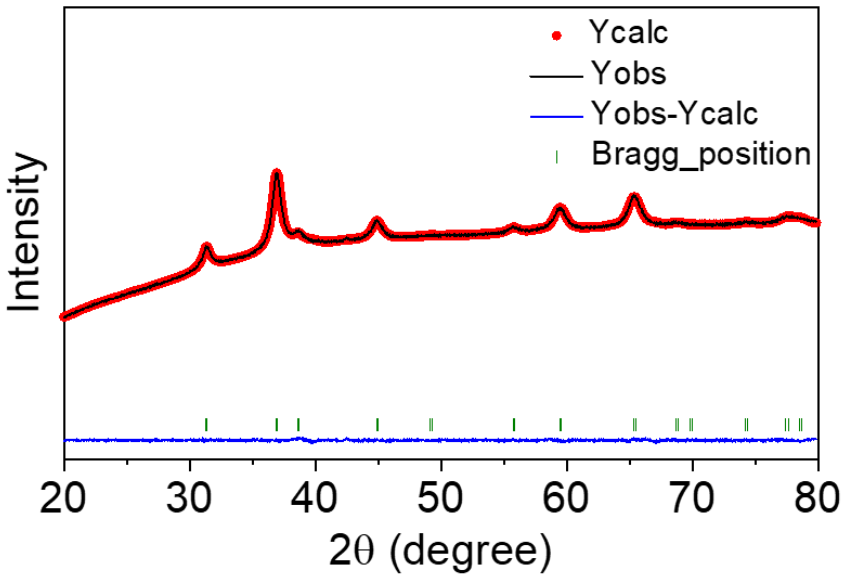


**Supplementary Figure 5**. Rietveld refinements of XRD patterns on as-synthesized $Co_3O_4$.

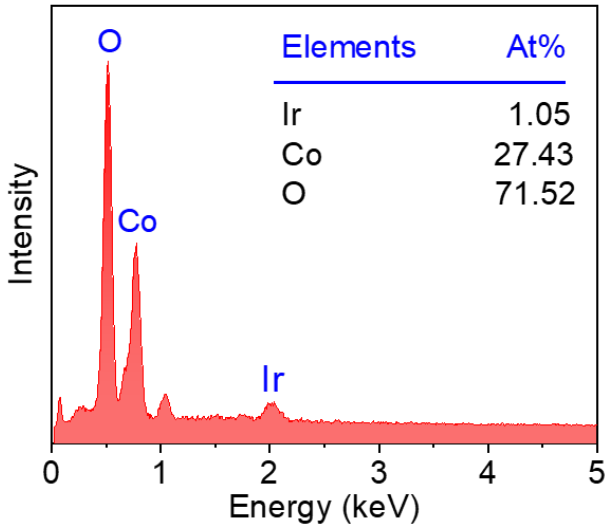


**Supplementary Figure 6.** SEM-EDS spectrum of Ir-$Co_3O_4$.

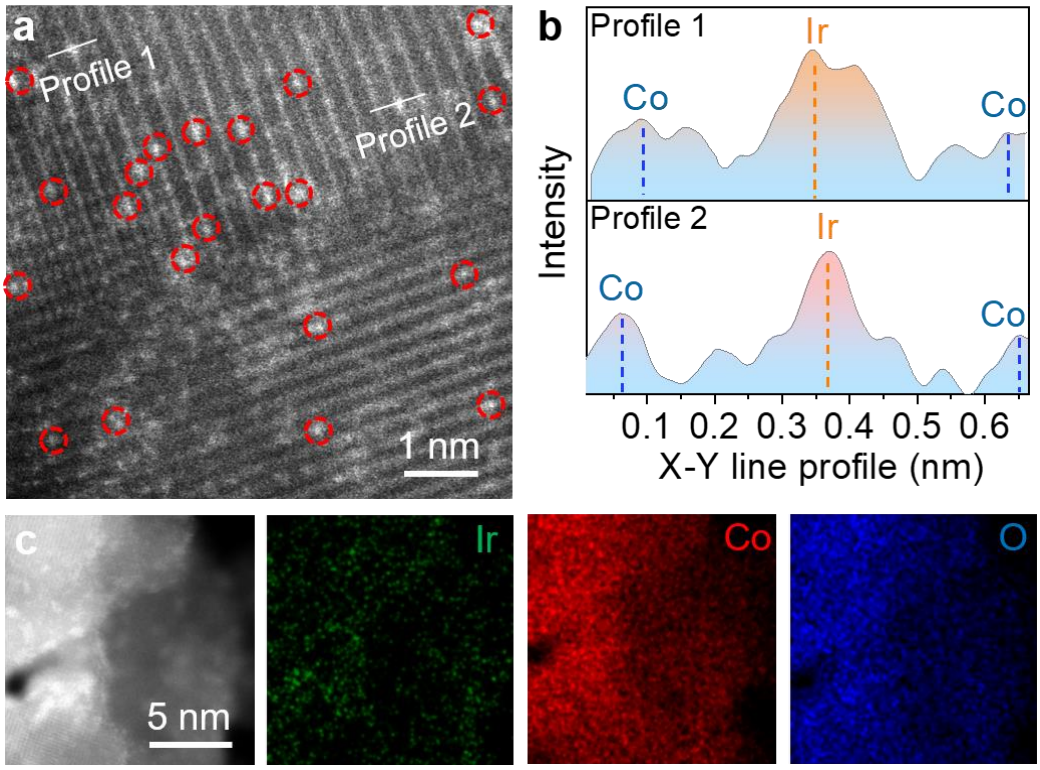


**Supplementary Figure 7.** (a) AC HAADF-STEM image of Ir-$Co_3O_4$. (b) The intensity profiles along the dash lines in (a). (c) AC HAADF-STEM image and the corresponding elemental mappings of Ir-$Co_3O_4$.

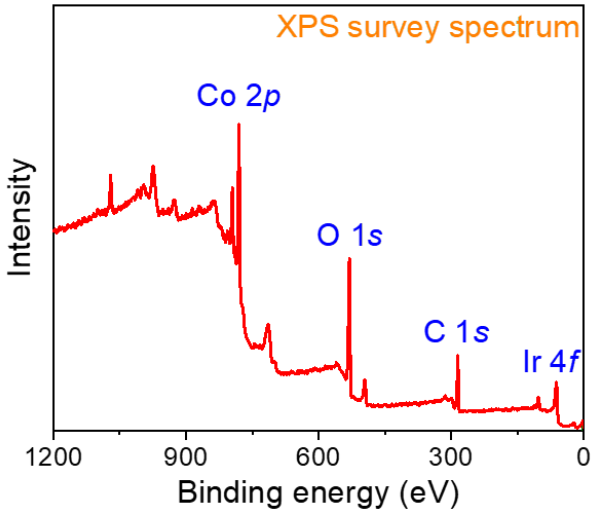


**Supplementary Figure 8.** XPS survey spectrum of Ir-$Co_3O_4$.

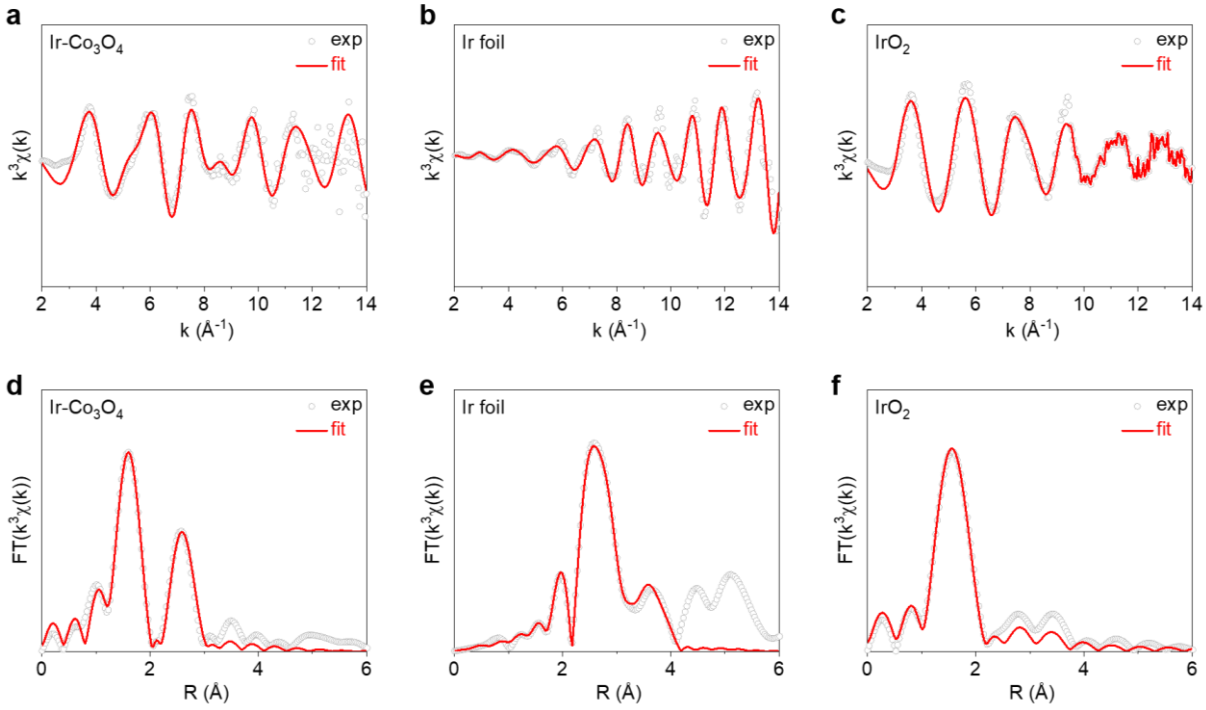


**Supplementary Figure 9.** (a-c) $k^3$-weighted k-space Ir $L_3$-edge experimental and fitting spectra of Ir-$Co_3O_4$ and references. (d-e) Corresponding $k^3$-weighted R-space Ir $L_3$-edge experimental and fitting spectra of Ir-$Co_3O_4$ and references.

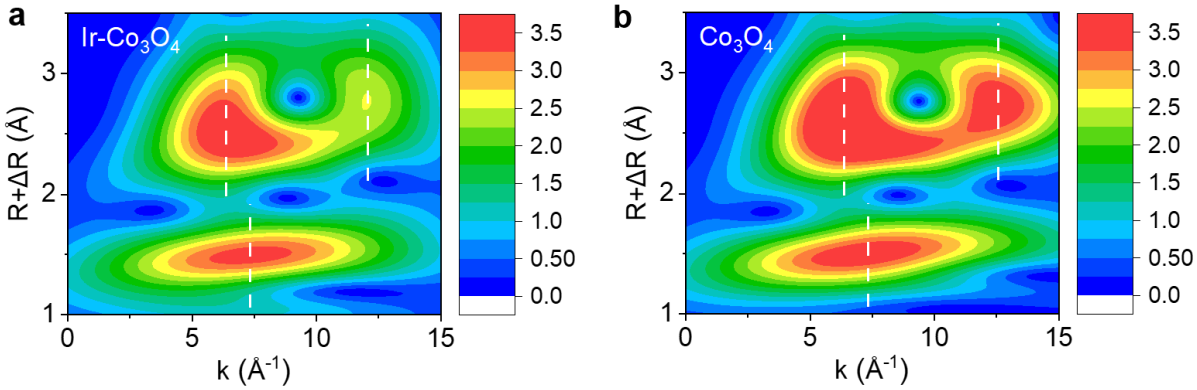


**Supplementary Figure 10.** WT-EXAFS analysis of Co *K*-edge on (a) Ir-$Co_3O_4$ and (b) $Co_3O_4$.

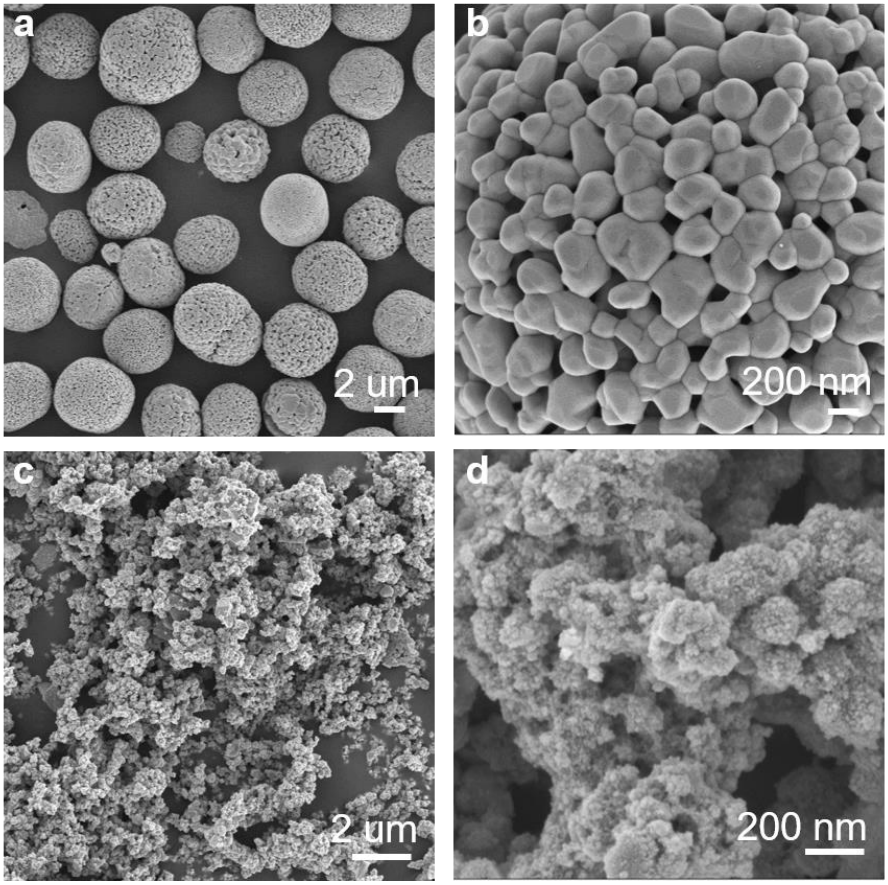


**Supplementary Figure 11.** SEM images of (a, b) commercial $Co_3O_4$ and (c, d) commercial $IrO_2$.

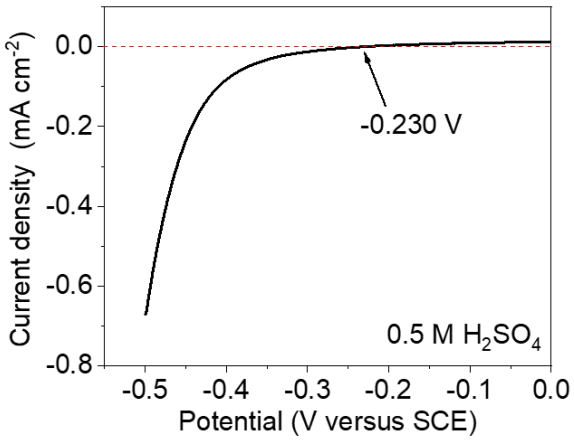


**Supplementary Figure 12.** Potential calibration of the calomel reference electrode at 25 ℃ in $H_2$-saturated 0.5 M $H_2SO_4$ solution.

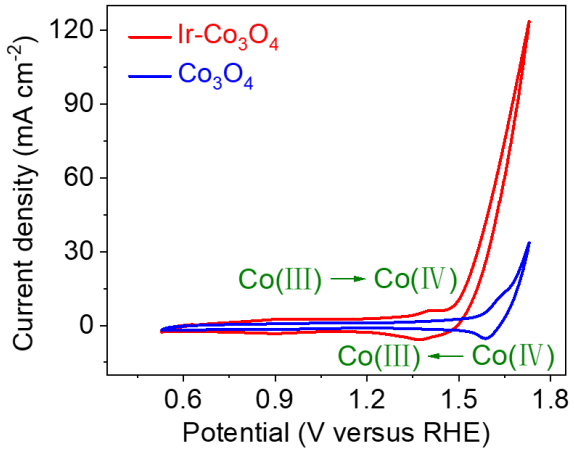


**Supplementary Figure 13.** CV curves within the Co redox potential range on Ir-$Co_3O_4$ and $Co_3O_4$ in 0.5 M $H_2SO_4$. Scan rates are 50 mV $s^{-1}$.

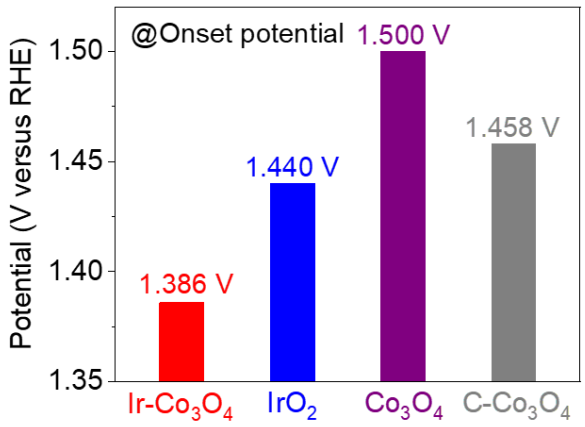


**Supplementary Figure 14.** The onset potentials for OER on Ir-$Co_3O_4$, $IrO_2$, $Co_3O_4$ and C-$Co_3O_4$.

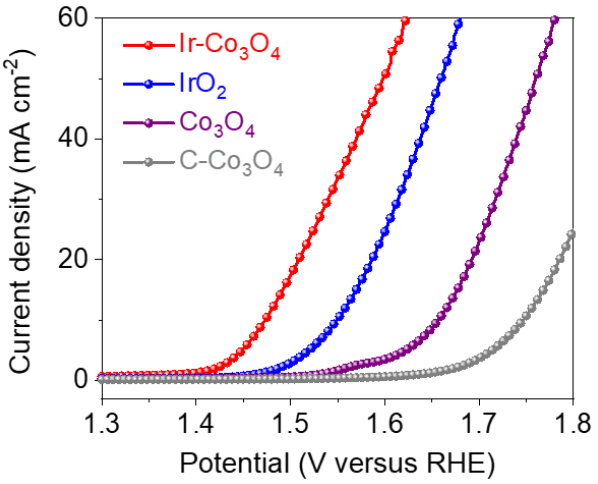


**Supplementary Figure 15.** Polarization curves without 95% iR compensation on Ir-$Co_3O_4$, $IrO_2$, $Co_3O_4$ and C-$Co_3O_4$ in 0.5 M $H_2SO_4$ at a scanning rate of 5 mV $s^{-1}$.

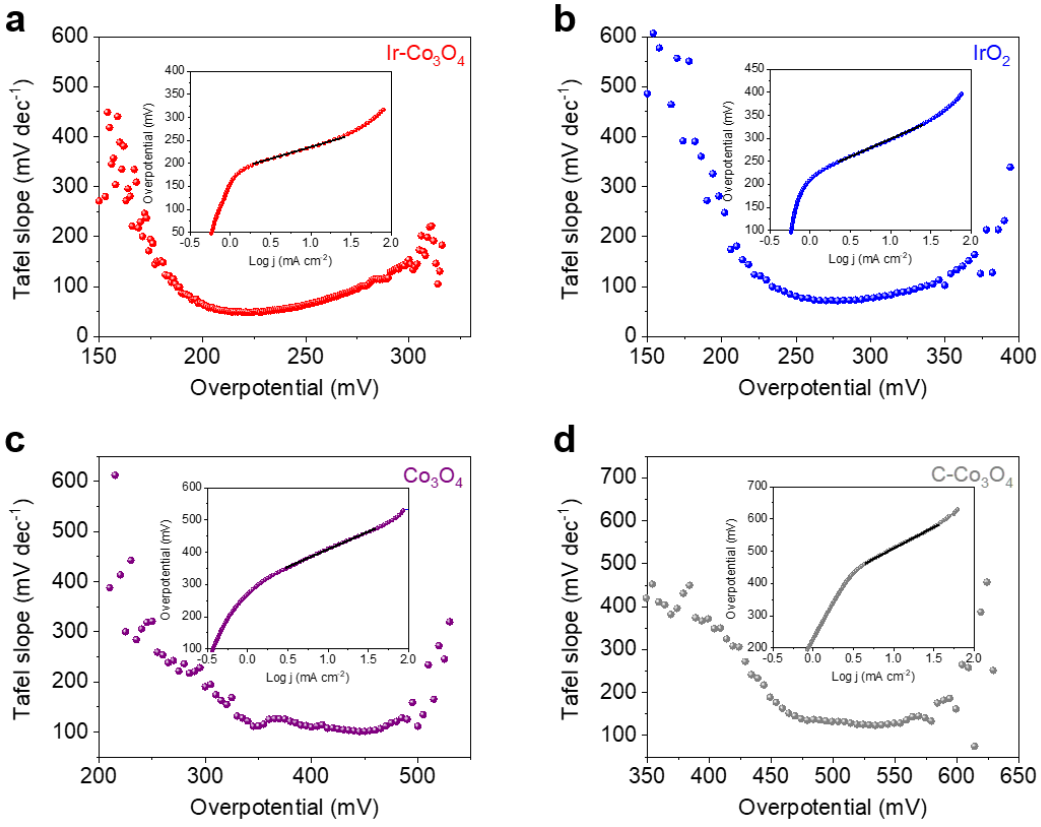


**Supplementary Figure 16.** The graphs that plot Tafel slope as a function of overpotential on (a) Ir-$Co_3O_4$, (b) $IrO_2$, (c) $Co_3O_4$ and (d) C-$Co_3O_4$. Insets are the Tafel plots of these catalysts.

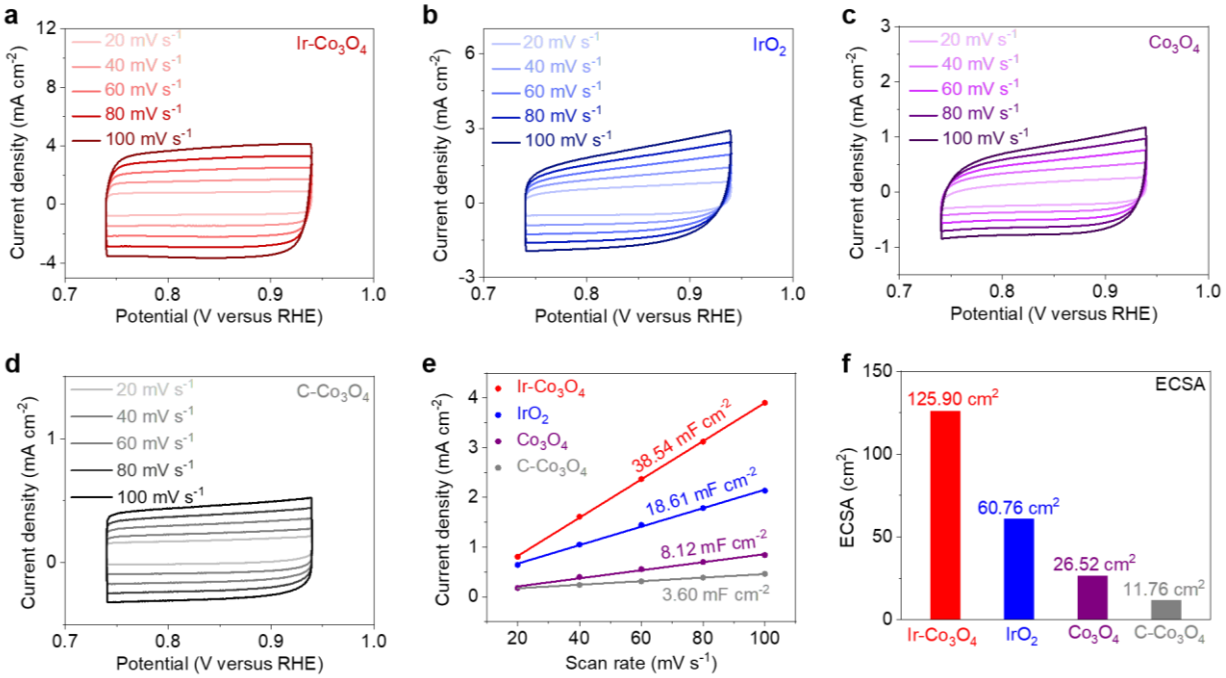


**Supplementary Figure 17.** Electrochemical cyclic voltammetry scans recorded for (a) Ir-$Co_3O_4$, (b) $IrO_2$, (c) $Co_3O_4$ and (d) C-$Co_3O_4$. Scan rates are 20, 40, 60, 80 and 100 mV $s^{-1}$. (e) Linear fitting of the capacitive currents versus cyclic voltammetry scans for these catalysts. (d) The calculated ECSA values for Ir-$Co_3O_4$, $IrO_2$, $Co_3O_4$ and C-$Co_3O_4$.

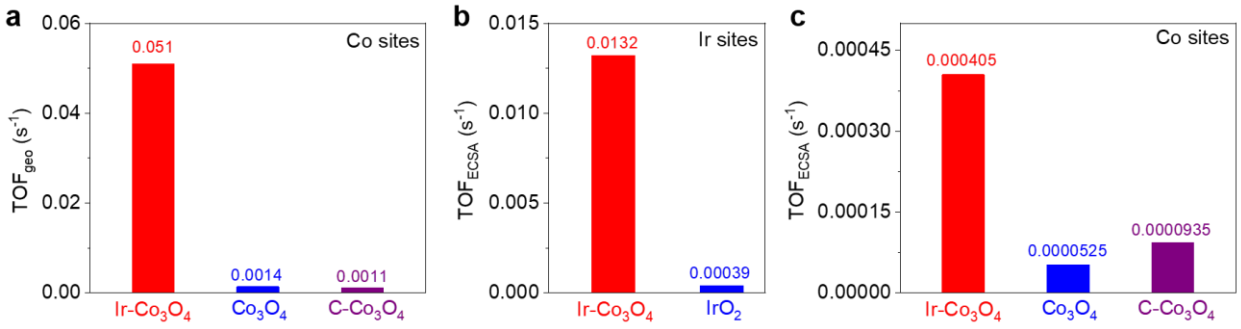


**Supplementary Figure 18.** (a) The TOF values that normalized to Co sites per geometric area of Ir-$Co_3O_4$, $Co_3O_4$ and C-$Co_3O_4$. The calculated TOF values that normalized to (a) Ir sites on Ir-$Co_3O_4$ and $IrO_2$ and (b) Co sites on Ir-$Co_3O_4$, $Co_3O_4$ and C-$Co_3O_4$ per ECSA.

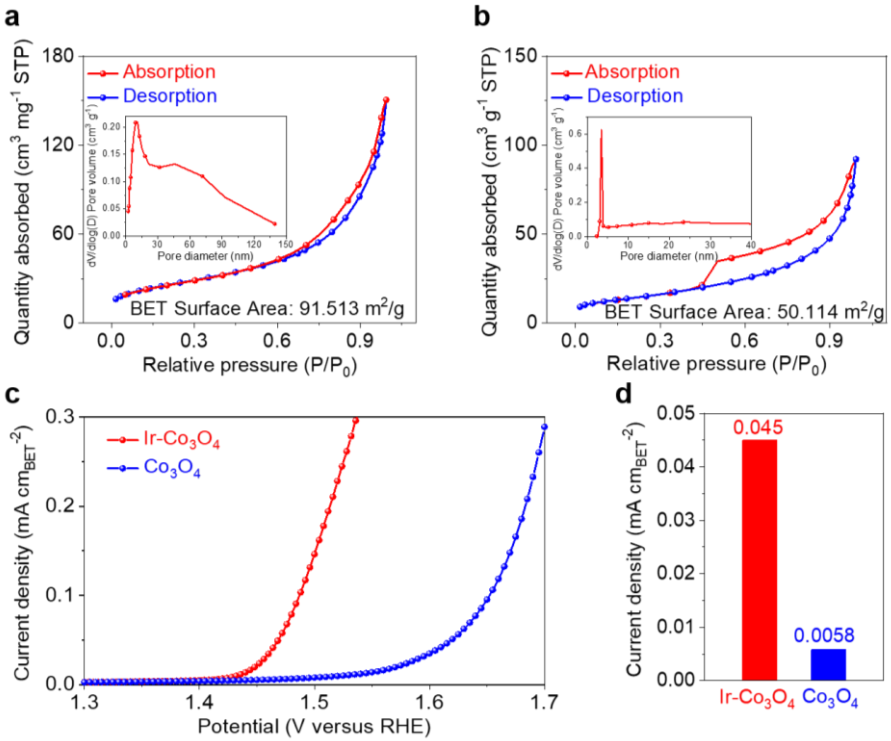


**Supplementary Figure 19.** $N_2$ absorption-desorption isotherms of (a) Ir-$Co_3O_4$ and (b) $Co_3O_4$. (c) The polarization curves normalized to BET surface areas and (d) corresponding normalized current densities of Ir-$Co_3O_4$ and $Co_3O_4$ at the overpotential of 236 mV.

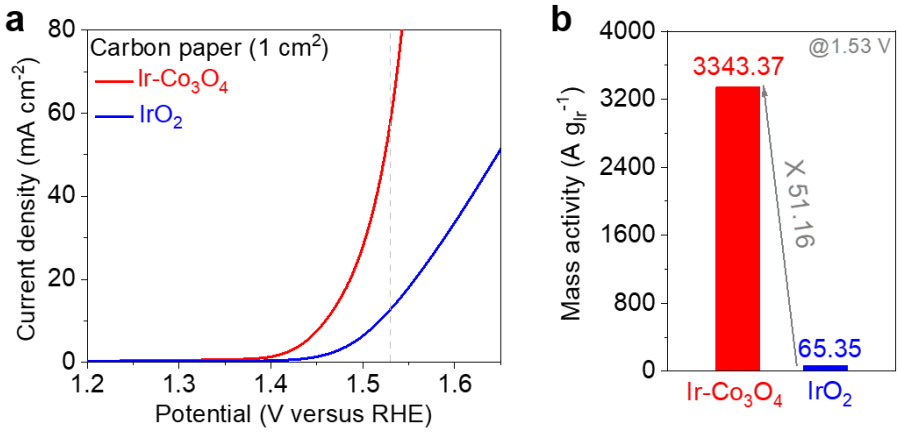


**Supplementary Figure 20.** (a) The OER polarization curves of Ir-$Co_3O_4$ and $IrO_2$ collected on the carbon paper electrode. (b) Corresponding mass activities of these catalysts at overpotential of 300 mV.

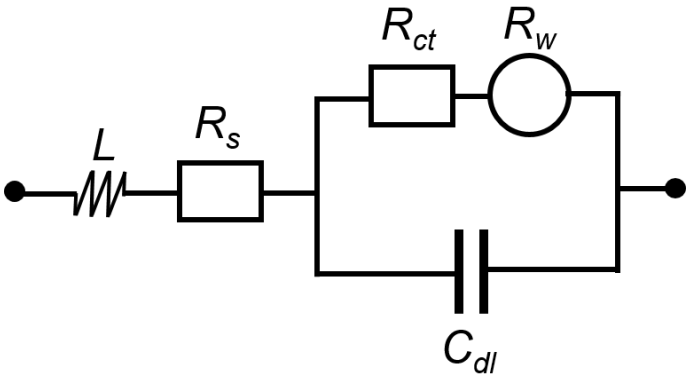


**Supplementary Figure 21.** The equivalent circuit applied in the EIS tests of these catalysts.

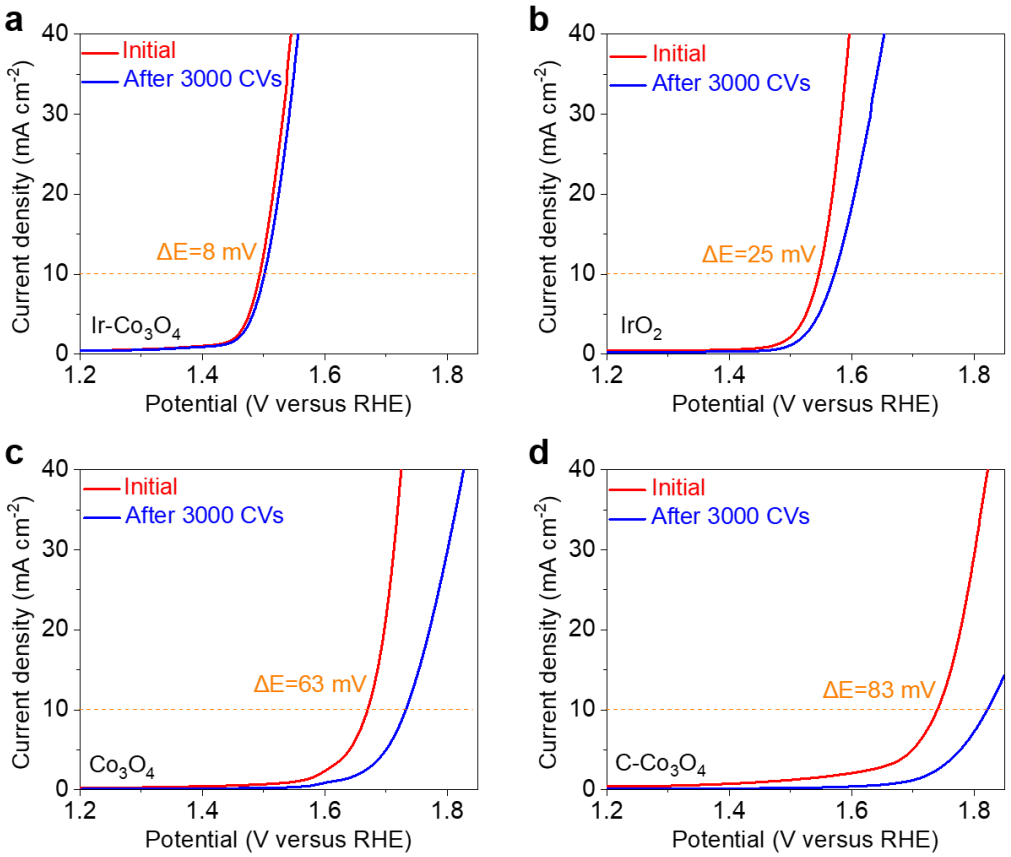


**Supplementary Figure 22.** Polarization curves of (a) Ir-$Co_3O_4$, (b) $IrO_2$, (c) $Co_3O_4$ and (d) C-$Co_3O_4$ before and after 3000 CV cycles in 0.5 M $H_2SO_4$ solution

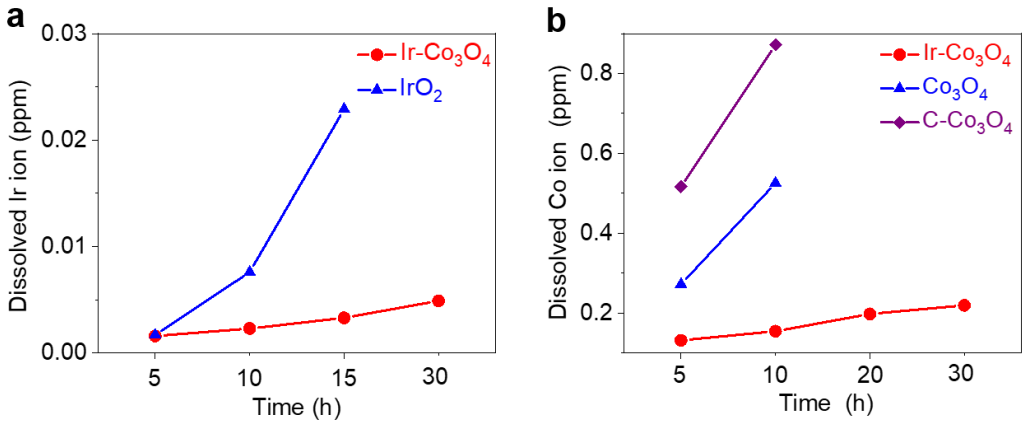


**Supplementary Figure 23.** (a) The dissolved Ir ion concentrations measured for Ir-$Co_3O_4$ and $IrO_2$, and (b) the dissolved Co ion concentrations measured for Ir-$Co_3O_4$, $Co_3O_4$ and C-$Co_3O_4$ in electrolyte during the chronopotentiometry at 10 mA $cm^{-2}$ by ICP-OES.

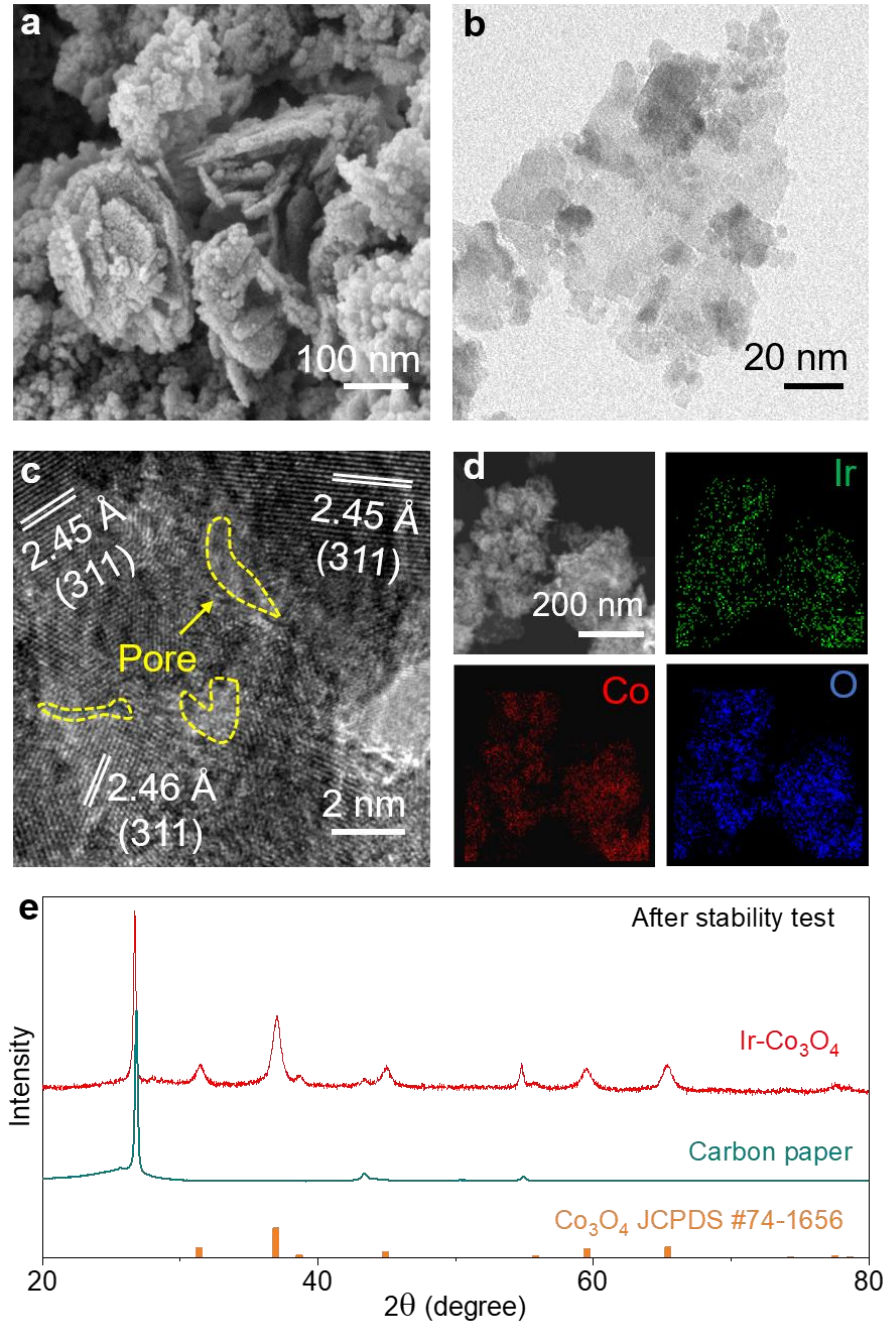


**Supplementary Figure 24.** Corresponding (a) SEM image, (b) TEM image, (c) HRTEM image, (d) elemental mappings and (e) XRD pattern of Ir-$Co_3O_4$ after stability test. Yellow circles represent the defective pores on Ir-$Co_3O_4$.

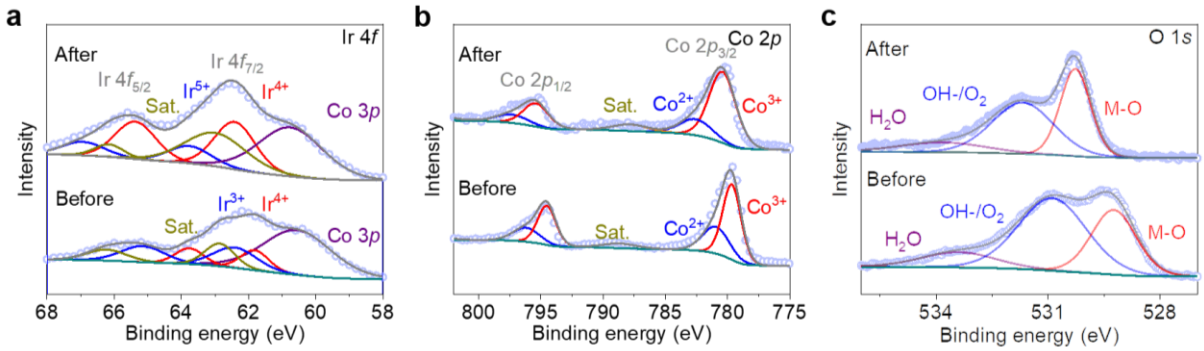


**Supplementary Figure 25.** Corresponding (a) Ir 4*f*, (b) Co 2*p*, (c) O1*s* XPS spectrum of Ir-$Co_3O_4$ before and after stability test.

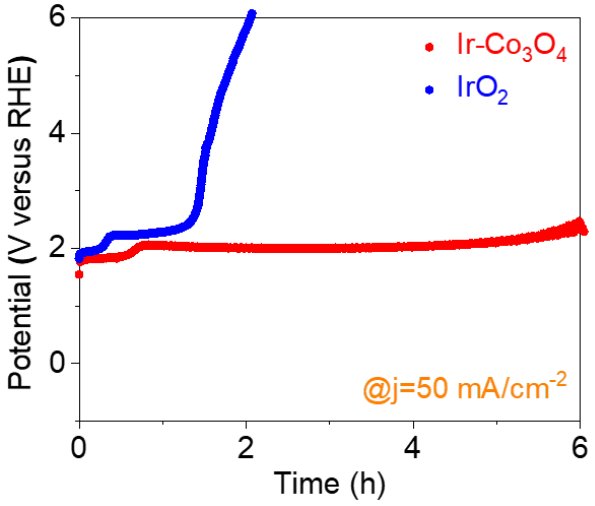


**Supplementary Figure 26.** Chronopotentiometric measurements of Ir-$Co_3O_4$ and $IrO_2$ at 50 mA $cm^{-2}$, carbon paper was used as the catalyst support.

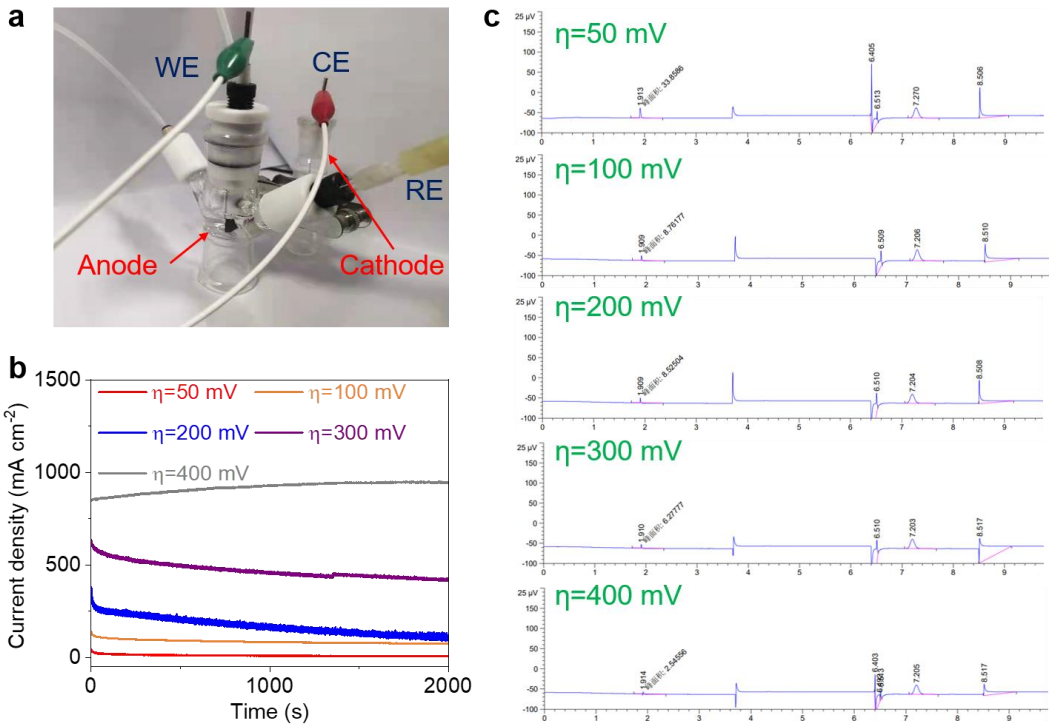


**Supplementary Figure 27.** (a) The setup used for conducting the OER on Ir-$Co_3O_4$ and was connected to GC to detect the amount of generated $O_2$. (b) Corresponding I-t curves of Ir-$Co_3O_4$ under various overpotentials for 2000s. (c) The GC signals of generated $O_2$ amount detected under various overpotentials on Ir-$Co_3O_4$.

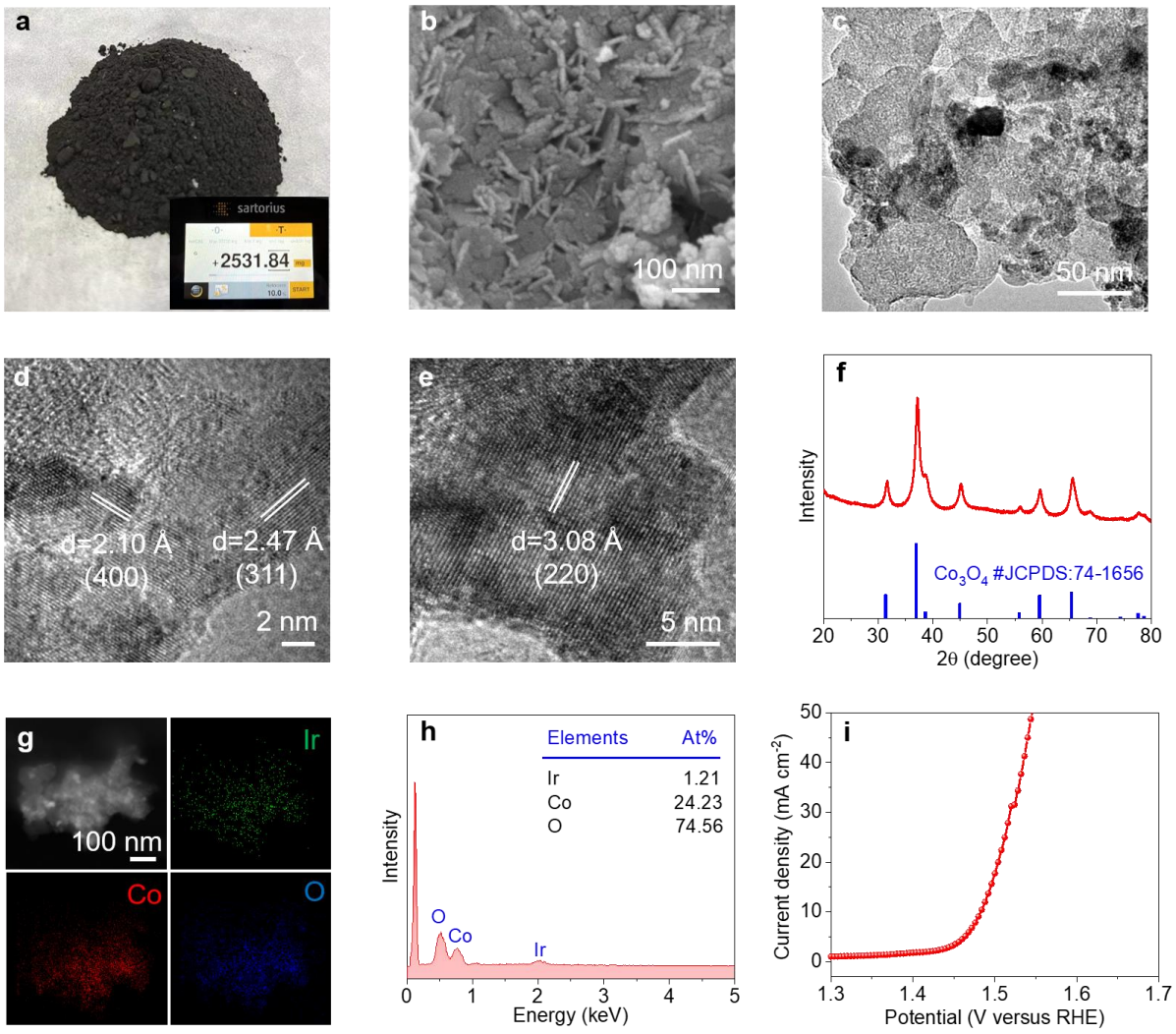


**Supplementary Figure 28.** (a) Digital photo, (b) SEM image, (c) TEM image, (d,e) HRTEM images, (f) XRD pattern, (g) elemental mappings, (h) SEM-EDS spextra and (i) polarization curves of the scale-up Ir-$Co_3O_4$.

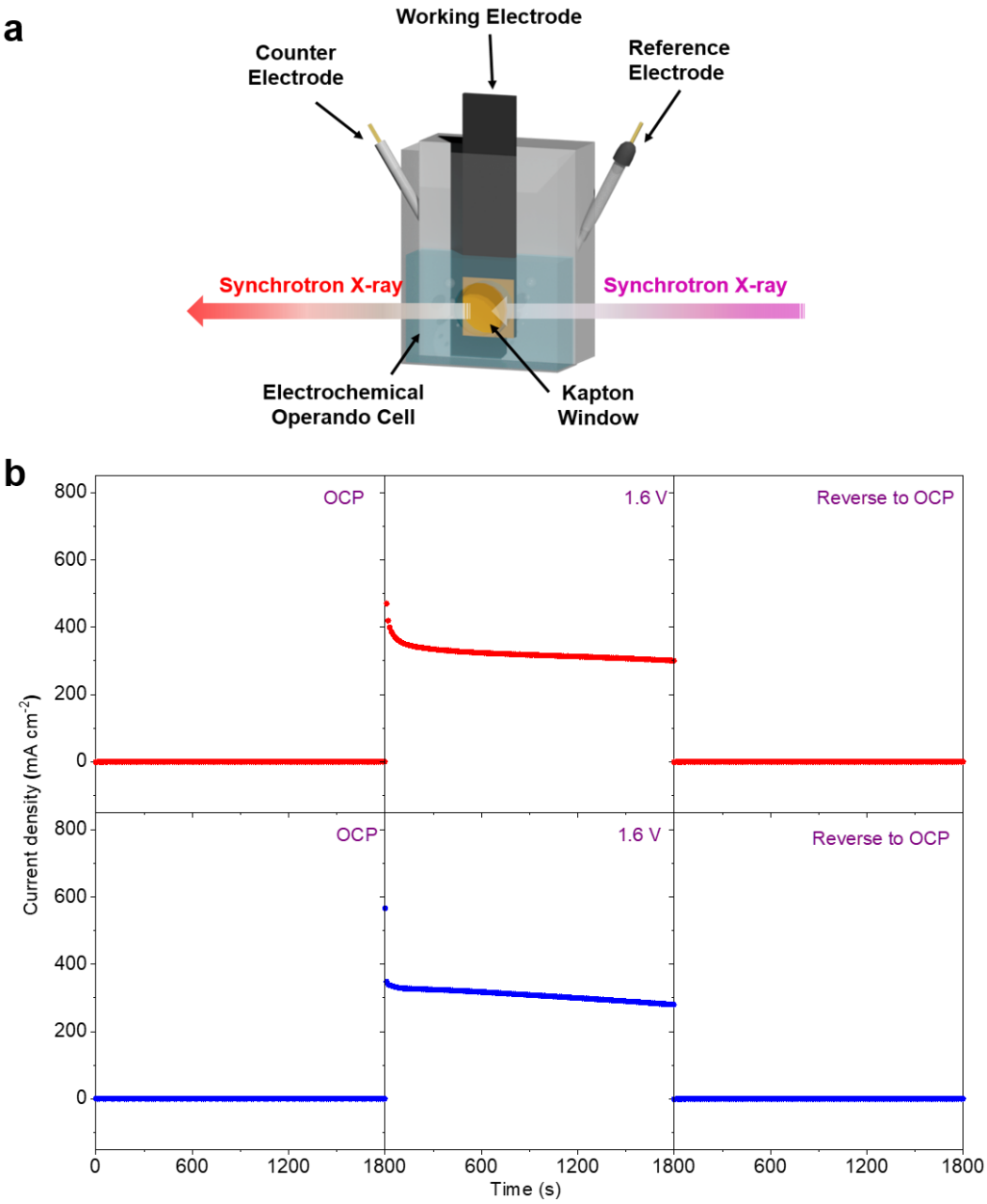


**Supplementary Figure 29.** (a) The schematic diagram of the custom-built electrochemical cell for operando XAS test. (b) The i-t curves were sequentially obtained under the applied potentials of OCP, 1.6 V and the reverse to OCP again, the Ir-$Co_3O_4$ was maintained under each potential for 1800 s. Red curves were conducted in the home-built electrochemical cell for collecting the operando XAS data and blue curves were conducted in the lab cell under the same condition for comparison, only slight difference can be distinguished between them.

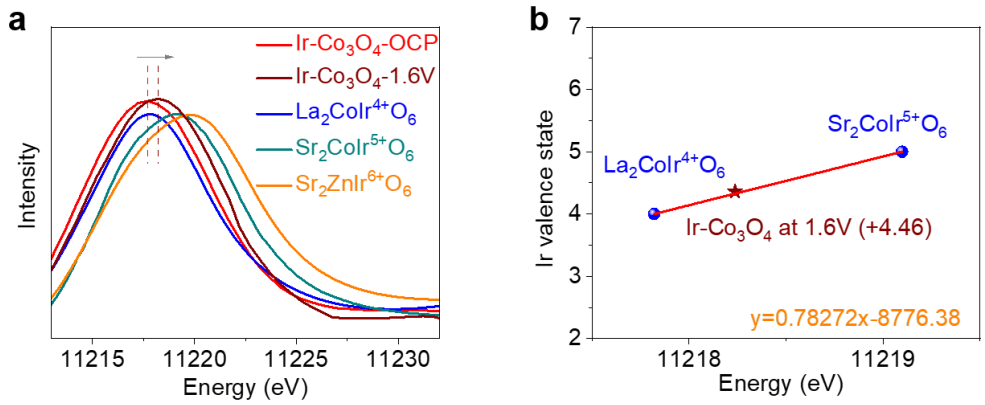


**Supplementary Figure 30.** (a) Operando Ir-$L_3$ XANES spectra of Ir-$Co_3O_4$ at OCP and 1.6 V. $La_2CoIrO_6$, $Sr_2CoIrO_6$ and $Sr_2ZnIrO_6$ represent the $Ir^{4+}$, $Ir^{5+}$ and $Ir^{6+}$ references, respectively. (b) Ir valence state-absorption energy standard curves determined by $La_2CoIrO_6$ and $Sr_2CoIrO_6$, and the calculated Ir valence state of Ir-$Co_3O_4$ at 1.6 V.

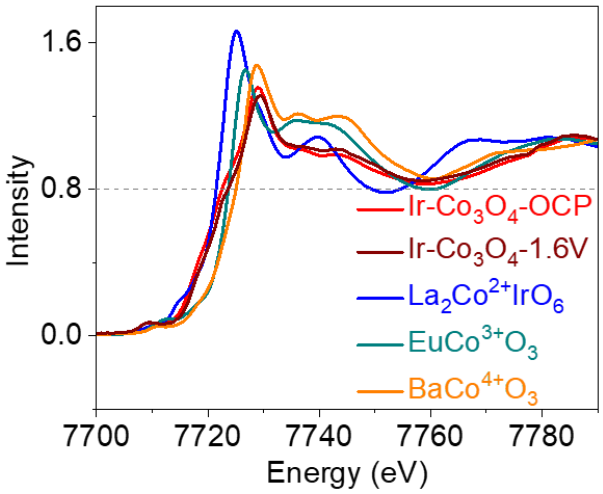


**Supplementary Figure 31.** Operando Co-$K$ XANES spectra of Ir-$Co_3O_4$ at OCP and 1.6 V. $La_2CoIrO_6$, $EuCoO_3$ and $BaCoO_3$ represent the $Co^{2+}$, $Co^{3+}$ and $Co^{4+}$ references, respectively.

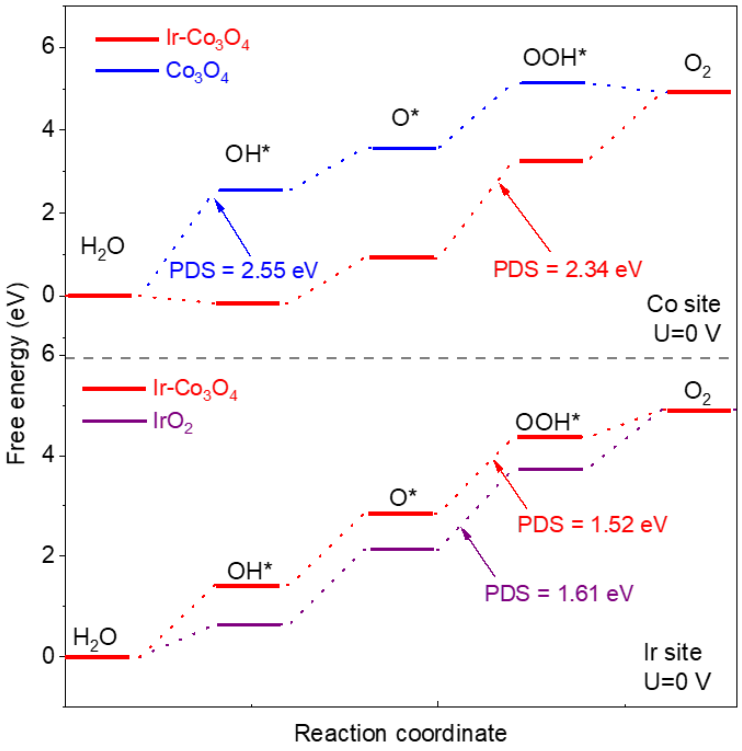


**Supplementary Figure 32.** The Gibbs free energy diagrams of the four-electron OER process on the Ir sites and Co sites of these catalysts under the applied overpotentials of 0 V vs. RHE, respectively.

**Supplementary Table 1.** Results of XRD refinements for Ir-$Co_3O_4$ and $Co_3O_4$.

| Compounds | *a* (Å) | *b* (Å) | *c* (Å) | *V* (Å$^3$) |
|---|---|---|---|---|
| Ir-$Co_3O_4$ | 8.097 | 8.097 | 8.097 | 530.9 |
| $Co_3O_4$ | 8.075 | 8.075 | 8.075 | 526.6 |

**Supplementary Table 2.** Fit goodness and R-factor of XRD refinements for Ir-$Co_3O_4$ and $Co_3O_4$.

| Compounds | $\chi^2$ | $R_F$ | $R_B$ | $R_P$ | $R_{WP}$ |
|---|---|---|---|---|---|
| Ir-$Co_3O_4$ | 1.78 | 0.412% | 0.561% | 10.1% | 6.41% |
| $Co_3O_4$ | 1.34 | 0.771% | 0.919% | 15.6% | 9.05% |

**Supplementary Table 3.** EXAFS fitting parameters of Ir-$Co_3O_4$, Ir foil and $IrO_2$.

| Compounds | Path | N | S02 | $\sigma^2$ / Å$^2$ | R / Å | ΔE0 | R-factor |
|---|---|---|---|---|---|---|---|
| Ir-$Co_3O_4$ | Ir-O1 | 1.685 | 0.759 | 0.00779± 0.009 | 1.769± 0.0985 | 6.396 | 0.00207 |
| | Ir-O2 | 3.370 | 1.519 | 0.00409± 0.003 | 1.968± 0.0222 | | |
| | Ir-O-Co | 3.290 | 1.464 | 0.01115± 0.005 | 2.910± 0.0251 | | |
| Ir foil | Ir-Ir1 | 12 | 0.638 | 0.00269± 0.003 | 2.707± 0.0033 | 6.717 | 0.0065 |
| | Ir-Ir2 | 6 | 0.638 | 0.00246± 0.001 | 3.838± 0.0725 | | |
| $IrO_2$ | Ir-O | 6 | 0.901 | 0.00650± 0.003 | 2.012± 0.0206 | 9.881 | 0.0186 |
| | Ir-Ir | 2 | 0.901 | 0.00801± 0.009 | 3.151± 0.0746 | | |

**Supplementary Table 4.** Comparisons of the Tafel slopes and overpotentials at the current density of 10 mA $cm^{-2}$ of reported Ir-based catalysts for OER in 0.5 M $H_2SO_4$.

| Catalysts | Overpotential (mV) | Tafel slope (mV $dec^{-1}$) | Ref. |
|---|---|---|---|
| Ir-$NiCo_2O_4$ NSs | 240 | 60 | 1 |
| $IrO_2$/GCN | 276 | 57 | 2 |
| $IrO_x$/9R-$BaIrO_3$ | 230 | 80 | 3 |
| $Ru_3Ir_1O_X$ | 231 | 93.2 | 4 |
| $Rh_{22}Ir_{78}$ | 292 | 101 | 5 |
| Ir@Fe/NCNT | 250 | 58.2 | 6 |
| DO-$IrTe_2$ | 298 | 49.4 | 7 |
| $Au_{0.5}Ir_{0.5}$ | 257 | 77.6 | 8 |
| $Ir_6Ag_9$ NTs | 285 | 61.1 | 9 |
| Mesoporous Ir NSs | 240 | 49 | 10 |
| P-$IrO_X$@DG | 290 | 67.5 | 11 |
| $IrO_2$ | 298 | 82 | **This work** |
| Ir-$Co_3O_4$ | 236 | 52.6 | |

**Supplementary Table 5.** Fitting parameters of EIS for Ir-$Co_3O_4$, $IrO_2$, $Co_3O_4$ and C-$Co_3O_4$.

| Samples | $R_s$ (Ω) | $R_{ct}$ (Ω) | $C_{dl}$ (F $s^{n-1}$) | s (Ω $s^{-1/2}$) |
|---|---|---|---|---|
| Ir-$Co_3O_4$ | 4.41 | 2.37 | 0.0001 | 0.001 |
| $IrO_2$ | 4.24 | 4.18 | 0.015 | 0.0015 |
| $Co_3O_4$ | 4.80 | 20.55 | 0.005 | 0.001 |
| C-$Co_3O_4$ | 4.31 | 115.5 | 0.001 | 0.001 |

## Supplementary References


1. Yin, J. et al. Iridium single atoms coupling with oxygen vacancies boosts oxygen evolution reaction in acid media. *J. Am. Chem. Soc.* **142**, 18378-18386 (2020).
2. Chen, J. et al. Low-coordinate iridium oxide confined on graphitic carbon nitride for highly efficient oxygen evolution. *Angew. Chem. Int. Ed.* **58**, 12540-12544 (2019).
3. Li, N. et al. Identification of the active-layer structures for acidic oxygen evolution from 9R-$BaIrO_3$ electrocatalyst with enhanced iridium mass activity. *J. Am. Chem. Soc.* **143**, 18001-18009 (2021).
4. He, J., Zhou, X., Xu, P. & Sun, J. Regulating electron redistribution of intermetallic iridium oxide by incorporating Ru for efficient acidic water oxidation. *Adv. Energy Mater.* **11**, 2102883 (2021)
5. Guo, H. et al. Rational design of rhodium-iridium alloy nanoparticles as highly active catalysts for acidic oxygen evolution. *ACS Nano* **13**, 13225-13234 (2019).
6. Luo, F. et al. Robust and stable acidic overall water splitting on Ir single atoms. *Nano Lett.* **20**, 2120-2128 (2020).
7. Pi, Y. et al. Selective surface reconstruction of a defective iridium-based catalyst for high-efficiency water splitting. *Adv. Funct. Mater.* **30**, 2004375 (2020).
8. Hu, H. et al. Electronically delocalized Ir enables efficient and stable acidic water splitting. *J. Mater. Chem. A* **8**, 20168 (2020).
9. Zhu, M., Shao, Q., Qian, Y. & Huang, X. Superior overall water splitting electrocatalysis in acidic conditions enabled by bimetallic Ir-Ag nanotubes. *Nano Energy* **56**, 330-337 (2019).
10. Jiang, B. et al. Mesoporous metallic iridium nanosheets. *J. Am. Chem. Soc.* **140**, 12434-12441 (2018).
11. Zhuang, L. et al. Porous structure engineering of iridium oxide nanoclusters on atomic scale for efficient pH-universal overall water splitting. *Small* **17**, 2100121 (2021).